GDCh Research Article Angewandte International Edition Chemie www.angewandte.org

How to cite: *Angew. Chem. Int. Ed.* **2025**, *64*, e202419953
doi.org/10.1002/anie.202419953

Metal-Oxo Species

Bridging the Oxo Wall: A New Perspective on High-valent Metal-Oxo Species and Their Reactivity in Mn, Fe, and Co Complexes

*Asmita Sen[+], Sunita Sharma[+], and Gopalan Rajaraman**

Abstract: The "oxo-wall" is a well-established concept in the area of bioinorganic chemistry, which refers to the instability of the terminal metal-oxo complexes in the +4 oxidation state, with tetragonal C_{4v} symmetry beyond group 8 elements. This leads to a diverse and highly reactive chemistry of Co-oxo complexes, as evidenced in the literature, ranging from challenging C–H bond activation to efficient water oxidation. Despite extensive research on first-row terminal metal-oxo complexes and the "oxo-wall" concept, studies correlating the reactivity of these species across the periodic table remain scarce. In this work, using a combination of DFT and ab initio CASSCF calculations, we have explored the structure, bonding, and reactivity of $[M^{IV/V}(15\text{-TMC})(O)(CH_3CN)]^{m+}$ (M = Mn, Fe and Co) species. Our study reveals several intriguing outcomes: (i) while existing literature typically indicates the presence of either $Co^{IV}=O$ or $Co^{III}–O^{\bullet}$ species beyond the wall, we propose a quantum mechanical mixture of these two species (termed as $Co^{IV}=O \leftrightarrows Co^{III}–O^{\bullet}$), with the per cent of mixing dictated by ligand architecture and symmetry considerations; (ii) we observe that the oxyl radical character increases beyond the wall, correlating with larger N_{trans}-M–O tilt angles; and (iii) we identify an inverse relationship between the percentage of $M–O^{\bullet}$ character and the kinetic barriers for C–H bond activation. These findings offer a new perspective on the roles of oxidation states, spin states, and the nature of the metal ion in reactivity.

Introduction

In terminal metal-oxo complexes, the oxo group acts as a potent π-donor, facilitating the formation of multiple metal-oxygen (M–O) bonds with early transition metals, such as the triple bond in d^1 VO^{2+}, low-spin d^2 CrO_2^{+}, and MoO_2^{+} ions.[1] As one progresses along the transition metal series to d^3-manganese (Mn^{IV}) and d^4-iron (Fe^{IV}), the gradual accumulation of unpaired d-electrons begins to populate the antibonding π* orbitals (π*-d_{xz} or π*-d_{yz}, Figure 1a), leading to a decrease in M–O π-bonding character, resulting in a bond order of *ca.* 1. This reduction in π-bonding strength contributes to the high reactivity and complex chemistry associated with the high-valent Mn/Fe/Co=O unit, which is an integral part of the active site of several haem[2] and non-haem[2f,3] metalloenzymes as well as biomimetic models. The frontier molecular orbital diagram in tetragonal M-oxo complexes with C_{4v} symmetry follows the energy ordering as $\sigma(M–O) < \pi_x(M–O) = \pi_y(M–O) < nb(d_{xy}) < \pi^*(d_{xz}) = \pi^*(d_{yz}) < \sigma^*(d_{x^2-y^2}) < \sigma^*(d_{z^2})$, where the first three orbitals are mostly ligand-centred and the latter five are with metal character. When one advanced from group 8 to group 9, the fifth unpaired electron moved into a π* antibonding orbital, diminishing the π-bond order, resulting in bond order approaching ~0.5 in tetragonal d^5-Co-oxo complexes. This alteration in electronic structure renders the oxo group highly basic and more susceptible to a proton or electrophilic attack.[1b] The scarcity of late transition metal-oxo complexes beyond group 8 in a high oxidation state (+4) in tetragonal geometry and their enhanced reactivity was first noted by Ballhausen and Gray and is known as the "oxo-wall" concept and became one of the celebrated concepts in bioinorganic chemistry.[4] The existence of free terminal $L_5Co^{IV}=O$ complexes is rare;[5] however, their potential formation as reactive intermediates cannot be overlooked. Due to their aggressive reactivity, these species have attracted significant interest from inorganic chemists, with an aim to design a true octahedral C_{4v} symmetric $Co^{IV}=O$ species by violating the "oxo-wall" concept[5a,6] (Scheme 1).

Despite numerous arguments[3j,7] and counterarguments[5b] about violating the "oxo-wall," the theoretical understanding remains limited, offering room for further study. The debate continues, with some pursuing a true $Co^{IV}=O$ species and others viewing it as $Co^{III}–O^{\bullet}$ without a formal double bond. From a multiconfigurational standpoint, our recent study has demonstrated that in a tetragonal environment, terminal metal-oxo species in the +4 oxidation state struggle to achieve a true $Co^{IV}=O$ form, regardless of geometric deviations.[8] In other words, it is neither $Co^{IV}=O$ nor $Co^{III}–O^{\bullet}$ but a quantum mechanical mixture of both species at different propositions (Figure 1b). Further, there is a precedent to this proposal by Maltempo and co-workers, who have proposed in heme proteins there is a quantum mechanical mixture of $S=^3/_2$ states with other states exists[9] (Figure 1c). Despite the initial precedence on the concept of quantum mechanical mixture, a significant

[*] Dr. A. Sen,[+] Dr. S. Sharma,[+] Prof. G. Rajaraman
Department of Chemistry
Indian Institute of Technology Bombay
IIT Bombay, Powai – 400076, Mumbai, Maharashtra, India
E-mail: rajaraman@chem.iitb.ac.in

[+] Both authors contributed equally to this work.

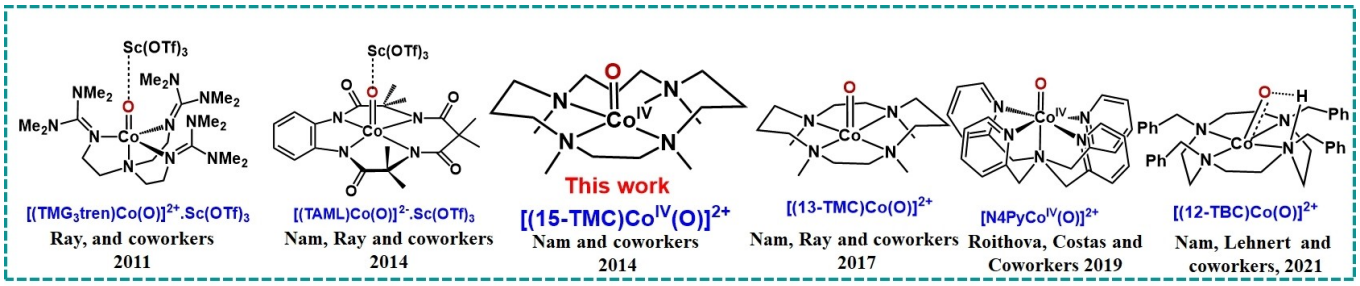

Scheme 1. A list of putative $Co^{IV}=O$ species reported to date, featuring various ligand architectures.

gap remains in the exploration of this hypothesis, which has not yet been pursued with the urgency it merits.[9b]

As we proceed through the transition metal series, in high valent metal-oxo complexes, the distinct presence of O(2p) bonding and metal 3d-orbitals diminishes[10] due to the gradual stabilisation of the d-orbitals. This enhances the mixing between the metal and ligand-centred orbitals and facilitates electronic transitions between them. Our earlier study proportionally linked this mixing to the reactivity of C–H bond activation.[11] A parallel can be drawn between these electronically excited states and the valence tautomers, represented as $\{M^{IV}=O \leftrightarrow M^{III}–O^{\bullet}\}$, which further can be tested as a catalyst towards the C–H bond activation process.[2d,12] This is also supported by some discrete literature that indicates the involvement of oxyl radical species during the C–H bond activation process, such as the role of $Mn^{III}–O^{\bullet}$ in photosystem II[13] and $Fe^{III}–O^{\bullet}$ in α-ketoglutarate-dependent non-heme halogenase metalloenzymes.[14] As mentioned earlier, the extremely short lifetimes of the species after the oxo-wall limit understanding the origin or their intricate reactivity.[5b] This complexity underscores the necessity of identifying a universal factor that governs the intricate dynamics of transition states, both before and beyond the oxo-wall, which will be critical for advancing catalyst design and improving reactivity control in these systems.

In this study, we have employed DFT and ab initio CASSCF calculations to explore the roles of $M^{IV/V}=O$ and $M^{III/IV}–O^{\bullet}$ species, examining how factors such as oxidation state, spin state, and d-electronic configuration influence the C–H bond activation reactivity. Particularly, we have investigated the reactivity of $Co^{IV}=O/Co^{III}–O^{\bullet}$ and $Co^{V}=O/Co^{IV}–O^{\bullet}$ species derived from the $[Co^{II}(15\text{-TMC})(CH_3CN)]^{2+}$ (TMC = N-tetramethylated cyclam) complex, focusing on their reactivity towards intramolecular hydrogen atom abstraction (HAA) from a TMC-methyl group, leading to the formation of $[Co^{III}(15\text{-TMC-OCH}_2)]^{2+}$ species as the final product. While the $Co^{IV}=O/Co^{III}–O^{\bullet}$ species is formed in a homolytic cleavage of the O–O bond, the formation of the one-electron oxidised $Co^{V}=O/Co^{IV}–O^{\bullet}$ species is facilitated via heterolytic O–O cleavage in an acidic medium. This particular experimental work provides us with a complete set of various valance tautomeric species $\{Co^{IV}=O$ or $Co^{III}–O^{\bullet}\}$ and $\{Co^{V}=O$ or $Co^{IV}–O^{\bullet}\}$ to understand the electronic structure and reactivity of species in HAA reaction.[15] Further the corresponding $\{Fe^{IV}(O)\}^{2+}$ analogue

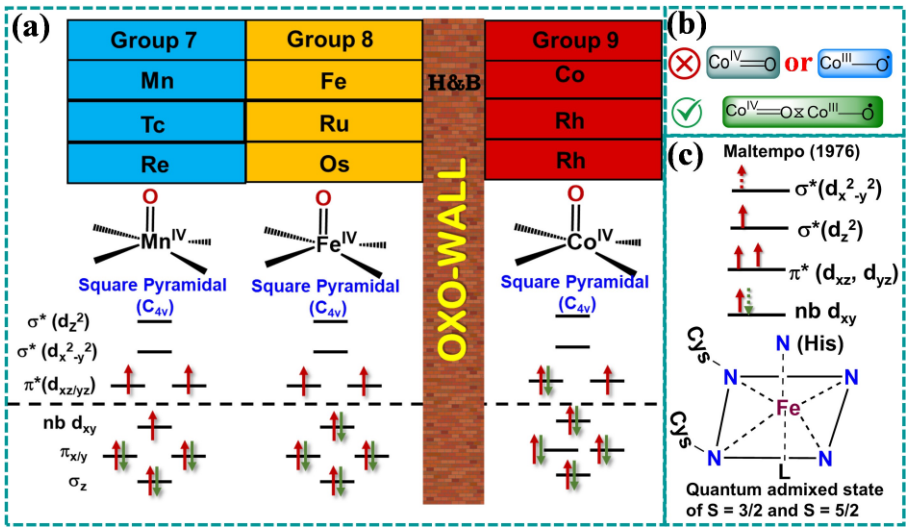

Figure 1. a) Splitting of d-orbital in Mn/Fe/$Co^{IV}=O$ species with C_{4v} geometry, (b) proposal on the existence of Co-oxo complexes as a quantum mechanical mixture of $Co^{IV}=O$ and $Co^{III}–O^{\bullet}$ valance tautomer, and (c) the work of Maltempo and co-workers demonstrates the mixing of $S={}^3/_2$ and $S={}^1/_2$ states in cytochrome *c*' (RHP), with the dashed arrow indicating partial occupancy, see ref [9].

has also been reported exhibiting olefin epoxidation reaction,[16] which led us to extend our studies to Fe and Mn analogues to characterise the actual active species during the hydrogen abstraction process before and beyond the oxo wall.

Results and Discussion

All DFT calculations are carried out at the uB3LYP/6-31G*(non-metals) + LanL2DZ (metals) // def2-TZVP (PCM-acetonitrile) level, with benchmarking performed at the uB3LYP/def2-TZVP (PCM-acetonitrile) level (see ESI), yielding similar trends (Figure S1–S3, and Table S1–S3). We performed calculations on the formation of metal-oxo species from the precursor complex $[M^{II}(15\text{-TMC})(CH_3CN)]^{2+}$ (*R*), which reacts with O_2 to form the metal-peroxo species $[M^{III}(15\text{-TMC})(O_2)]^{+}$ (*int1*). Upon protonation to $[M^{III}(15\text{-TMC})(OOH)]^{2+}$ (*int2*) and subsequent O–O bond cleavage, the reaction thermodynamically favours the formation of stable $M^{IV}=O/M^{III}–O^{\bullet}$ species, consistent with experimental observations (see ESI for details, Scheme S1, Figure S4–S10, and Table S4–S9).[8,15]

Ab Initio Quantification of the Quantum Mechanical Mixture of $M^{IV/V}=O$ vs $M^{III/IV}–O^{\bullet}$ Species

Both the $[(15\text{-TMC})Mn(O)(CH_3CN)]^{2+}$] (*int3*$_{a\text{-}Mn}$) and $[(15\text{-TMC})Fe(O)(CH_3CN)]^{2+}$] (*int3*$_{a\text{-}Fe}$) species possess a high-spin ground state, $S=^3/_2$ and $S=^5/_2$ respectively, with a close-lying $S=^3/_2$ state for Fe (4.5 kJ/mol), while in Mn, the low-spin state lies at 67.6 kJ/mol.[8,15] The Co-analogue, $[(15\text{-TMC})Co(O)(CH_3CN)]^{2+}$] (*int3*$_{a\text{-}Co}$) possesses a $S = ^3/_2$ as the ground state with a $S=^1/_2$ excited states at 17.9 kJ/mol. Further, S = 1, S = 2 and $S = ^3/_2$ were computed as the ground state for *int3*$_{b\text{-}Mn}$, *int3*$_{b\text{-}Co}$ and *int3*$_{b\text{-}Fe}$, respectively. Other spin-states are lying significantly higher in energy (> 60 kJ/mol); therefore, we have eliminated them from further discussion (Figure 2 and Figures S1–S3).

The ground-state geometries of all *int3*$_a$ and *int3*$_b$ species exhibit pseudo-C_s symmetry, except for *int3*$_{b\text{-}Co}$, which lacks symmetry due to a significantly elongated Co–N_{eq} bond (3.320 Å). The tetragonal C_{4v} symmetry of these complexes is lifted due to the addition of a methylene group at the periphery of the cyclam ligand (Figure S8 and S10). In the ground state optimised geometry of ^{4}*int3*$_{a\text{-}Mn}$ (^{3}*int3*$_{b\text{-}Mn}$), ^{3}*int3*$_{a\text{-}Fe}$ (^{4}*int3*$_{b\text{-}Fe}$), and ^{4}*int3*$_{a\text{-}Co}$ (^{5}*int3*$_{b\text{-}Co}$) species, the M–O bond lengths are estimated to be 1.633 (1.658) Å, 1.606

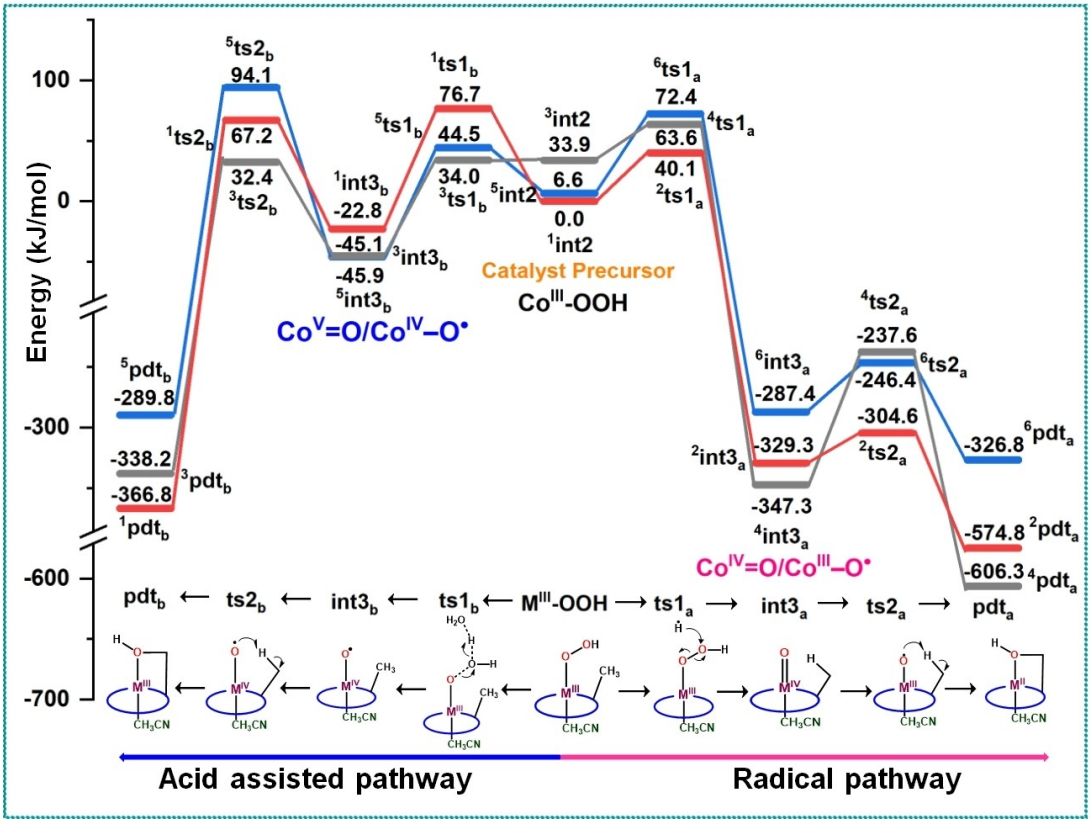

Figure 2. Energy profile diagram for the formation of $[LCo^{IV}=O\leftrightarrow LCo^{III}–O^{\bullet}]$ and $[LCo^{V}=O\leftrightarrow LCo^{IV}–O^{\bullet}]$ species from ***int2*** (a M^{III}-hydroperoxo species) and their reactivity towards C–H bond (see Scheme S1). The pink and blue arrows starting from ***int2*** represent two different pathways; the right side is the radical pathway and the left side is the acid-assisted pathway. Energies are in kJ/mol. The final free energies (ΔG) are derived from uB3LYP/def2-TZVP calculations with acetonitrile solvent.

(1.607) Å, and 1.594 (1.623) Å, respectively. The M–N_{eq} distances were found to lie within the range of 2.1 Å - 2.3 Å. The deviation from linearity in the N_{trans}–M–O bond angle is 2.4° (9.1°) for $^{4}int3_{a\text{-}Mn}$ ($^{3}int3_{b\text{-}Mn}$), 0.6° (1.6°) for $^{3}int3_{a\text{-}Fe}$ ($^{4}int3_{b\text{-}Fe}$), and 1.1° (13.0°) for $^{4}int3_{a\text{-}Co}$ ($^{5}int3_{b\text{-}Co}$). The N_{trans}–M–O angle shows a significant deviation from linearity in $int3_{a\text{-}Mn}$, while it remains nearly linear in $^{3}int3_{a\text{-}Fe}$ and $^{4}int3_{a\text{-}Co}$. In the $int3_b$ series, $^{5}int3_{b\text{-}Co}$ exhibits the largest deviation, followed by $^{3}int3_{b\text{-}Mn}$, with $^{4}int3_{b\text{-}Fe}$ showing near-linear geometry. The elongated M–O bond in $int3_b$ ($int3_a$) is reflected in the Badger corrected[17] Mn–O, Fe–O, and Co–O stretching frequencies ν(M–O) of 717 (929) cm^{-1}, 912 (910) cm^{-1}, and 754 (883) cm^{-1}, respectively. These values are generally consistent with the experimentally reported stretching frequencies.[18,12j,19,20],[21,22] Looking simply at the M–O bond length and associated stretching frequencies reveals that while the $int3_a$ resembles $M^{IV}=O$ form, the $Mn^{V}=O$ has a dominant Mn^{IV}–O• character (Table S10–S11).

The DFT computed spin density values on the oxyl radical centres in both $int3_a$ and $int3_b$ are significantly higher, >0.5 in all species (Figure S8 and S10), indicating the complexes have dominant $M^{III/IV}$–O• character. To explore the functional dependency of the oxyl radical character in $int3_a$ and $int3_b$, we have performed benchmarking with the TPSSh, PBE0, and ω-B97xD functionals (see ESI for details). All functionals predicted a similar trend, with Co-oxo species showing the least sensitivity, followed by Fe and Mn (see Table S12). Given that DFT, as a single-determinant approach, cannot effectively capture multiconfigurational character in molecules, performing ab initio CASSCF calculations on these complexes is essential. This justification is reinforced by our previous work, where CASSCF studies on high-valent metal-oxo and hydroxo species revealed that excited states of the same spin multiplicity exhibited lower kinetic barriers—a phenomenon termed identical spin multistate reactivity (ISMR).[11]

At the equilibrium distance, the CAS(11,8) calculations on $^{4}int3_{a\text{-}Co}$ yield a 77.9 % contribution from $\sigma(p_z+d_z^2)^2\ \pi(p_y+d_{yz})^2\ \pi(p_x+d_{xz})^2\ \delta^*(d_{xy})^2\ \sigma^*(p_z+d_z^2)^1\ \pi^*(p_y+d_{yz})^1\ \delta^*(d_{x^2-y^2})^1\ \pi^*(p_x+d_{xz})^0$ configuration to the total ground state wavefunction with a smaller contribution (20.2 %) coming from a $\sigma(p_z+d_z^2)^1\ \pi(p_y+d_{yz})^2\ \pi(p_x+d_{xz})^1\ \delta^*(d_{xy})^2\ \sigma^*(p_z+d_z^2)^2\ \pi^*(p_y+d_{yz})^1\ \delta^*(d_{x^2-y^2})^1\ \pi^*(p_x+d_{xz})^1$ configuration (* represents the orbitals with dominant metal 3d-character. The configurations are one of the representative ones among various configurations of same type). The former corresponds to a classical $Co^{IV}=O$ form, and the latter for Co^{III}-O• valance tautomer (Table S13). The estimated contribution shows that the species has a dominant $Co^{IV}=O$ character in accordance with the prediction by the ν(Co–O) stretching frequency values. As these two species are quantum mechanically mixed and it is neither $Co^{IV}=O$ nor Co^{III}-O•, we suggest representing this a dual-curved arrow as $Co^{IV}=O$ ⧛ Co^{III}–O•.

The CAS(9,8) and CAS(10,8) calculations on the $^{4}int3_{a\text{-}Mn}$ and $^{5}int3_{a\text{-}Fe}$ show that 60.4 % and 77.3 % contributions arise from the $M^{IV}=O$ species, with 36 % and 22 % contributions from the oxyl radical forms, respectively. A greater deviation in the N_{trans}–M–O angle from the linearity in $int3_{a\text{-}Mn}$ is attributed to the Mn^{III}-O• dominance. In the low-lying first excited doublet state, the Co^{III}-O• electromeric species contribution was smaller (18.3 %). In $int3_b$, the scenario is reversed, the Co^{IV}-O• form having $\sigma(p_z+d_z^2)^2\ \pi(p_x+d_{xz})^2\ \delta^*(d_{xy})^2\ \pi(p_y+d_{yz})^1\ \pi^*(p_x+d_{xz})^1\ \sigma^*(p_z+d_z^2)^1\ \delta^*(d_{x^2-y^2})^1\ \pi^*(p_y+d_{yz})^0$ configuration is dominant (73.4 %), with a smaller contribution (23.3 %) from the $Co^{V}=O$ form ($Co^{V}=O$ ⧛ Co^{IV}–O•,Table S15). A similar trend is observed in $int3_{b\text{-}Mn}$ and $int3_{b\text{-}Fe}$ species, with the M^{IV}-O• tautomer contributing 54.9 % and 51.8 %, with the $M^{V}=O$ form accounting for 39.0 % and 47.1 % respectively. We have also calculated the EPR g, D, and E/D values, which are in agreement with the available experimental data (Table S14 in ESI). Furthermore, the quantum mechanical mixture, which is anticipated to affect the EPR parameters as previously demonstrated, along with various metrics such as g, D, E/D, and the hyperfine tensor, can be used to quantify this mixing.[3j,5b,18c,19c,23] Larger oxyl radical character can be quantified from the g-tensors, which, in the extreme case of 100 % Co^{III}-O•, is expected to be isotropic. Additionally, measuring the hyperfine coupling of using ^{17}O for the oxyl oxygen atom can help determine spin densities and the extent of quantum mechanical mixing.[23c]

The CASSCF-computed crystal field splitting (CFS) of d-based orbitals, representing the energy gap from the lowest to the highest d-orbitals, follows the trend: $^{4}int3_{a\text{-}Mn}$ (0.50 eV) < $^{4}int3_{a\text{-}Co}$ (0.70 eV) < $^{3}int3_{a\text{-}Fe}$ (0.84 eV) for $int3_a$, and $^{5}int3_{b\text{-}Co}$ (0.43 eV) < $^{3}int3_{b\text{-}Mn}$ (0.60 eV) < $^{4}int3_{b\text{-}Fe}$ (0.64 eV) for $int3_b$. The correlation between a larger N_{trans}–M–O tilt angle, reduced CFS, and enhanced oxyl radical character prompted us to explore their relationship with the HAA reaction and its associated barrier.

The Role of the "Oxo-Wall" in C–H Bond Activation

As intramolecular C–H bond activation has been reported for these catalysts, we have explored the mechanism where the metal-oxo species via a transition state ($ts2_a$ for radical pathway and $ts2_b$ for acid-assisted pathway) abstract the hydrogen atom from the N–Me group at the ligand periphery. This is followed by the formation of an oxetane-like product in the next step ($pdt_{a/b}$; see Scheme S1). For this reaction, the estimated lowest energy barriers (across various spin states) are 55.1 kJ/mol ($^{4}ts2_{a\text{-}Mn}$), 181.7 kJ/mol ($^{5}ts2_{a\text{-}Fe}$) and 42.7 kJ/mol ($^{2}ts2_{a\text{-}Co}$) from $int3_a$. These energies indicate that a minimum energy crossing point is required for Fe and Co, but not for Mn (Figure S1–S3). In the acid-assisted mechanism, with $int3_b$ as the active species, the C–H bond activation barriers are smaller for Mn and Fe compared to the corresponding barriers for $int3_a$ (17.9 kJ/mol for $^{3}ts2_{b\text{-}Mn}$ and 14.5 kJ/mol for $^{2}ts2_{b\text{-}Fe}$). In contrast, the energy barrier for the Co-analogue is substantially larger (78.3 kJ/mol for $^{3}ts2_{b\text{-}Co}$). Overall, the estimated C–H bond activation barrier exhibits the following trend $^{5}ts2_{a\text{-}Fe}$ (181.7 kJ/mol) > $^{3}ts2_{b\text{-}Co}$ (78.3 kJ/mol) > $^{4}ts2_{a\text{-}Mn}$ (55.1 kJ/mol) > $^{2}ts2_{a\text{-}Co}$ (42.7 kJ/mol) > $^{3}ts2_{b\text{-}Mn}$ (17.9 kJ/mol) > $^{2}ts2_{b\text{-}Fe}$ (14.5 kJ/mol) (Figure 3). This unveils that Mn/Fe^{V}=O ⧛ Mn/

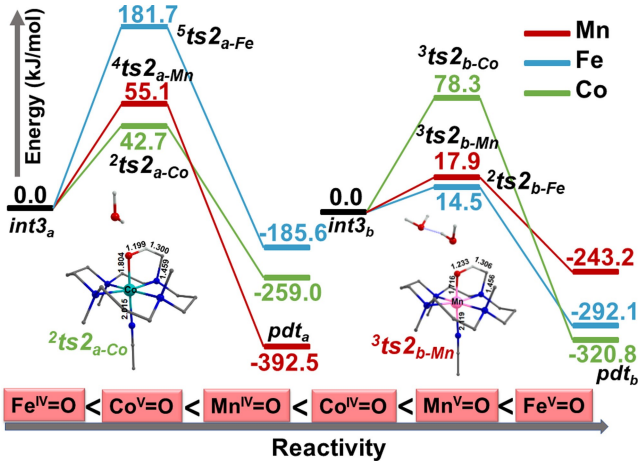

Figure 3. DFT-calculated energy profile diagram for intramolecular C–H bond activation in Mn, Fe, and Co-oxo species, referencing ***int3***$_{a/b}$ for the ground spin state (in ΔG, kJ/mol). The trend at the bottom shows the decreasing order of computed barrier heights for the individual species.

Fe^{IV}–O$^{\bullet}$ are highly reactive, while the Fe in a dominant form of Fe^{IV}=O or Fe^{III}–O$^{\bullet}$ exhibit sluggish reactivity. Co-analogue reactivity is found to be in between these two cases (Figure S11–S12). In the rate-determining transition states $ts2_{a\text{-}Mn}$, $ts2_{a\text{-}Fe}$, and $ts2_{a\text{-}Co}$, the DFT computed spin densities on the metal (activated carbon) centres are 3.792 (−0.304), 3.883 (−0.191), and 0.093 (0.492), respectively, indicating a concerted HAA mechanism.

Analysing the spin densities of the transition states relative to the corresponding reactant geometries reveals a diminishing oxyl radical character at the transition states. The extent of this reduction ($\Delta\rho = \rho(O)_{ts} - \rho(O)_R$) is 0.635 for Mn and 0.341 for Fe. This is accompanied by a concomitant increase of spin density at the metal centre, with 0.991 on Mn in $^4ts2_{a\text{-}Mn}$. This indicates that at $ts2_a$, a greater d(M)-O(p) mixing is observed for Mn, with the least mixing observed for Fe, leading to a lower barrier and higher reactivity for the Mn species arising from a stronger multi-configurational character. For $^3ts2_{b\text{-}Mn}$, $^2ts2_{b\text{-}Fe}$, and $^3ts2_{b\text{-}Co}$ species, the DFT computed spin densities on the carbon centre are −0.484, −0.400, and 0.472, respectively. This suggests a transfer of α-electron from the C–H bond to Mn and Fe, while a spin-down β-electron is transferred in Co. Although the transfer of β-electron in Co is reflected in the decrease in the residual spin on metal (1.508), there is no prominent increase in spin-density observed in Mn (0.104) and Fe (0.21). This is attributed to a net flow of beta spin density from p(O) → 3d(M), which is found to be highest in Mn (~0.2), while its negligible in Co (~0.01).

Our CASSCF calculations capture this scenario well in these transition states. In both $^4ts2_{a\text{-}Mn}$ and $^2ts2_{a\text{-}Co}$, the dominant M^{III}-O$^{\bullet}$ contribution is 64.7 %, and 69.7 %, respectively, with the following configurations: for Mn $\sigma(p_z+d_z^2)^2\ \pi(p_y+d_{yz})^2\ \pi^*(p_x+d_{xz})^2\ \delta^*(d_{xy})^1\ \delta^*(d_{x^2-y^2})^1\ \pi^*(p_y+d_{yz})^1\ \pi(p_x+d_{xz})^0\ \sigma^*(p_z+d_z^2)^0$ and for Co, $\sigma(p_z+d_z^2)^2\ \pi(p_y+d_{yz})^2\ \sigma^*(p_z+d_z^2)^2\ \pi(p_x+d_{xz})^1\ \pi^*(p_y+d_{yz})^2\ \delta^*(d_{xy})^1\ \delta^*(d_{x^2-y^2})^1\ \pi^*(p_x+d_{xz})^0$ (Table S15). The pure Mn^{IV}=O and Co^{IV}=O forms contribute smaller percentages of 30.6 % and 25.5 %, respectively. A completely reversed scenario is observed in $^5ts2_{a\text{-}Fe}$, where the ground state is composed of 69.6 % from Fe^{IV}=O form with a majorly contributing $\sigma(p_z+d_z^2)^2\ \pi(p_x+d_{xz})^2\ \pi(p_y+d_{yz})^2\ \delta^*(d_{xy})^1\ \sigma^*(p_z+d_z^2)^1\ \pi^*(p_y+d_{yz})^1\ \delta^*(d_{x^2-y^2})^1\ \pi^*(p_x+d_{xz})^0$ configuration along with a contribution of 27.1 % from the tautomeric Fe^{III}-O$^{\bullet}$ (Figure 4 and Table S13). The contribution from oxyl-radical tautomeric forms is found to be significantly enhanced in the one-electron oxidised $ts2_{b\text{-}Mn}$ and $ts2_{b\text{-}Fe}$. The CAS(10,8) calculations reveal a dominant $\pi(p_x+d_{xz})^2\ \pi(p_y+d_{yz})^2\ \sigma^*(p_z+d_z^2)^2\ \pi^*(p_y+d_{yz})^1\ \delta^*(d_{xy})^0\ \sigma(p_z+d_z^2)^0\ \pi^*(p_x+d_{xz})^1\ \delta^*(d_{x^2-y^2})^0$ configuration (80.4 %) with 11.8 % from Mn^{V}=O form in $^3ts2_{b\text{-}Mn}$. The contribution from

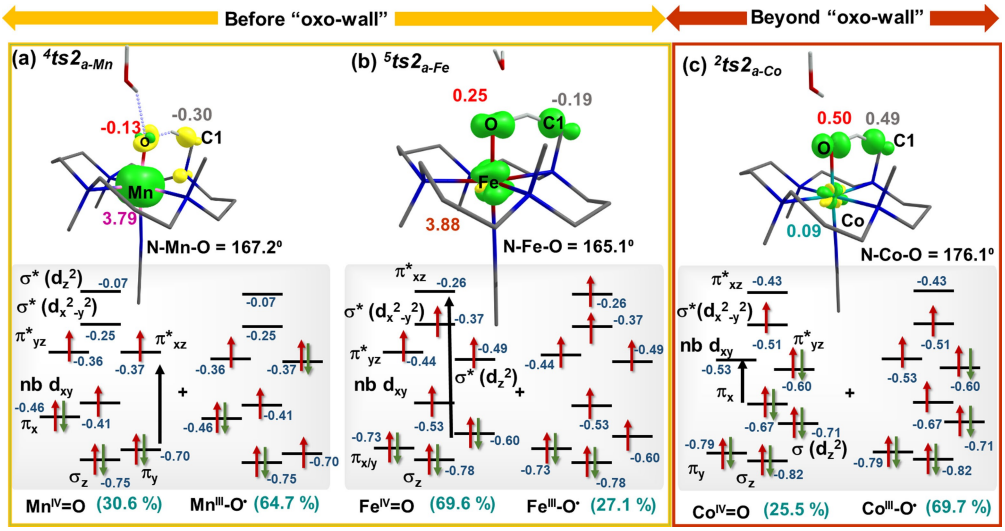

Figure 4. The DFT-computed spin density, along with CASSCF-calculated d-orbital splitting and the percentage of mixing, for (a) $^4ts2_{a\text{-}Mn}$, (b) $^5ts2_{a\text{-}Fe}$, and (c) $^2ts2_{a\text{-}Co}$. Note that only the major configurations contributing to M^{IV}=O and M^{III}–O$^{\bullet}$ forms are shown. The black arrows indicate transitions corresponding to tautomeric conversions (see Table S13–S14, energies in eV).

Fe^{IV}–O• tautomer is further increased in $^{2}ts2_{b\text{-}Fe}$ species, with negligible contribution from the Fe^{V}=O form. This remains similar in the Co analogous with Co^{IV}-O•, tautomeric form contributing lower to the overall mixed state (25.2 %).

To investigate the relationship between the transition state barriers, the two electromeric forms, and their quantum mechanical mixing, we performed a relaxed potential energy surface scan along the intramolecular C–H bond coordinate, where the C–H bond was elongated in steps of 0.05 Å up to 1.40 Å (1.45 Å for Mn) and compressed to 1.10 Å, specifically for three transition states: $^{3}ts2_{b\text{-}Mn}$ (lower energy barrier before the wall), $^{5}ts2_{a\text{-}Fe}$ (highest energy barrier), and $^{2}ts2_{a\text{-}Co}$ (intermediate energy barrier beyond the oxo wall)(Figure S13).

The overall scan reveals three distinct scenarios: at the lower C–H bond length region (1.2–1.25 Å), the percentage of mixing between M^{IV}=O and M^{III}–O• tautomers is expected to be similar to that observed for the reactants; at higher lengths (1.25–1.3 Å), the mixing closely resembles the transition states; and for C–H bond lengths greater than 1.3 Å, the mixing aligns more closely towards the estimate obtained for the product. To understand the change in the contribution from each tautomeric form, we have performed CASSCF calculations on each point. In $^{3}ts2_{b\text{-}Mn}$, the M^{III}-O• character is maximum (~60 %) at 1.3 Å (close to the C–H bond length is the transition state). With the compression of the C–H bond, the Mn^{V}=O character increases, reaching as high as 55 % at 1.1 Å, with a concomitant reduction in the M^{IV}–O• character (~42.5 %). When the bond is elongated from the equilibrium point, the M^{IV}–O• character remains almost similar. On the contrary, near the equilibrium point, the % M^{III}–O• character is minimum in $^{5}ts2_{a\text{-}Fe}$ and $^{2}ts2_{a\text{-}Co}$ (< 23 %). The contribution from this oxyl radical remains almost the same as the C–H bond is compressed, however, a significant increase is observed, reaching 69.5 % at 1.4 Å, as we elongate the bond. A similar trend is noticed in $^{2}ts2_{a\text{-}Co}$ species, where a maximum M–O• form is noticed at 1.35 Å. Therefore, at the extreme left of the scan, i.e., at the reactant-like structure, the M=O form is dominating, and at the extreme right i.e. at the product-like geometry, the M–O• form is dominant in all cases. This indicates that the energy barrier for the intramolecular HAA reaction is strongly dependent on the composition of the $M^{IV/V}$=O ⧖ $M^{III/IV}$–O• forms at the transition state (Figure 5, see Table S16 for optimised geometry coordinates).

Several metal-oxo species were reported to perform deformylation reactions after methyl hydroxylation.[24] To understand the possible deformylation reaction, we have performed additional mechanistic studies (see ESI for details, Scheme S2, Figure S14–S20), and this reveals that the barrier for the M–O bond cleavage is steeply high, preventing the formation of this product and this is consistent with experiments where the reaction found to stop at species pdt_a. Further, the deformylation product formation is also found to be endothermic and hence is not favoured thermodynamically.

Discussion

Although the H&B concept has been widely accepted in the scientific community for several decades, its applicability and manifestation during a chemical reaction remain unexplored, which motivates the present study. We would like to further note here that $M^{V/IV}$=O species are inherently a quantum mechanical mixture of the corresponding oxyl radical species, best represented using the dual-curved arrow notation, such as M^{IV}=O ⧖ M^{III}–O• and M^{V}=O ⧖ M^{IV}–O•, rather than as pure $M^{IV/V}$=O or the corresponding oxyl-radical electromers. The percentage of mixing between the M^{IV}=O and M^{III}–O• electromeric forms was found to be correlated to symmetry present in the complex along with the distortions in the geometry pertaining to the M–O bond. While in the one-electron reduced M–O species, the M^{IV}=O tautomeric form is dominant, in the one-electron oxidised M–O species, the dominant form is determined to be M^{IV}–O•, irrespective of the position of the metal, i.e. before or beyond the wall. Further, in addition to the electronic configurations, the oxidation state of the metal (correlated to the redox potential), along with its ligand architecture and geometry, dictates the dominant tautomeric form.

Since DFT lacks multiconfigurational accuracy, CASSCF is essential for capturing phenomena such as ISMR,[11] and here, this combination highlights the N_{trans}–M–O tilt angle as a key factor in determining the dominant species between $M^{IV/V}$=O and $M^{III/IV}$–O• tautomeric forms. While it is

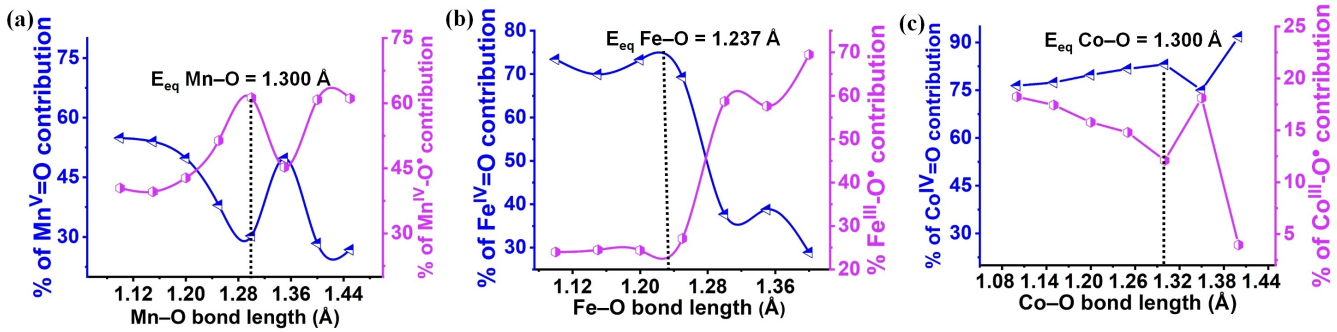

Figure 5. CASSCF-calculated percentage contributions of M=O and M–O• species in (a) $ts2_b$ of Mn complexes, (b) $ts2_a$ of the iron complex, and (c) $ts2_a$ of the cobalt complex as a function of the M–O distance.

intriguing to find this correlation to the extent of mixing between these two tautomers, the importance of this tilt angle in the reactivity of metal-oxo species has been witnessed earlier in non-haem $Fe^{IV}=O$ complexes towards hydrogen atom transfer reaction.[19a,25] Our calculations have shown that the higher the tilt N_{trans}–M–O angle, the larger the contribution of the oxyl radical form to the ground state wave function. As the tilt angle increases as ${}^5int3_{b\text{-}Co} > {}^3int3_{b\text{-}Mn} > {}^4int3_{b\text{-}Fe}$ and ${}^4int3_{a\text{-}Mn} > {}^4int3_{a\text{-}Co} > {}^3int3_{a\text{-}Fe}$, the overall crystal field splitting of d-orbitals decreases, narrowing the energy gap between ligand-centred and metal-centred molecular orbitals, which promotes their mixing. This resulting weak ligand field was found to facilitate electron transfer between metal and ligand-centred orbitals, leading to dominant $M^{III/IV}$–$O^{\bullet}$ character.[11] As the N_{trans}–M–O angle increases, this is expected to weaken the $\pi(d_{xz}\text{-}O_{px})$ and $\pi(d_{yz}\text{-}O_{py})$ bond order, leading to a more pronounced $M^{III/IV}$–$O^{\bullet}$ character. Previous studies have suggested that the oxo-wall is crucial for the instability of ideal terminal metal-oxo species in a tetragonal C_{4v} ligand environment.[5b] The present study emphasises that when the symmetry is disrupted by increasing the N_{trans}–M–O tilt angle, it promotes the formation of oxyl radical character rather than a true $M^{IV}=O$ species. As we continue to await the unambiguous characterization of $Co^{IV}=O$ species, such as through X-ray analysis, a ligand architecture designed in such a way that induces a least bent in N_{trans}–M–O angle could offer a path toward their stabilisation.

The mixing of the two tautomers drastically increased in $int3_{b\text{-}Mn}$ and $int3_{b\text{-}Fe}$ species except for the Co-analogue, which is mostly populated by the oxyl radical form. The H&B oxo-wall concept suggests that with the addition of an electron in the π* orbital beyond group 8, the M–O π-bond weakens, which increases the reactivity of a metal-oxo species due to the stabilisation of a Co^{III}–$O^{\bullet}$ form. If we consider this hypothesis to be true, in that case, based on the % of M=O vs M–$O^{\bullet}$ species, the reactivity should be, ${}^3ts2_{b\text{-}Co} > {}^3ts2_{b\text{-}Mn} > {}^2ts2_{b\text{-}Fe} > {}^4ts2_{a\text{-}Mn} > {}^2ts2_{a\text{-}Co} > {}^5ts2_{a\text{-}Fe}$. However, the calculated reactivity trend is ${}^2ts2_{b\text{-}Fe} > {}^3ts2_{b\text{-}Mn} > {}^2ts2_{a\text{-}Co} > {}^4ts2_{a\text{-}Mn} > {}^3ts2_{b\text{-}Co} > {}^5ts2_{a\text{-}Fe}$. ***This clearly suggests that even if the ground state geometry of the given complex has an ideal M=O form, during the transition state, it evolves with the greater proposition of M–O• species, which eventually performs the HAA reaction.*** Surprisingly, our findings reveal that the percentage of M–$O^{\bullet}$ radical character is inversely proportional to the kinetic barrier, regardless of the metal ion's spin state, oxidation state, or identity. This unexpected relationship challenges the extensive literature that emphasises the importance of spin and oxidation states in determining reactivity.

Conclusions

Our study challenges the long-accepted H&B concept by proposing that metal-oxo species exist as a quantum mechanical mixture of $M^{IV}=O$ and M^{III}–$O^{\bullet}$ forms, with the balance between these species influenced by geometric distortions, such as the N_{trans}–M–O tilt angle. We find that the greater the oxyl radical character (M^{III}–$O^{\bullet}$), the lower the kinetic barrier for reactivity, which highlights the critical role of structural factors, like tilt angle, in dictating the reactivity of these species, rather than solely their spin state or oxidation state.

Supporting Information

The Supporting Information contains computational details, optimised geometries, energy profile diagrams, spin density plot of reactant, transition states, intermediates state, and products of all stationary points and the relevant CASSCF data.

Acknowledgements

We thank SERB (SB/SJF/2019-20/12; CRG/2022/001697) for funding. AS/SS thank IITB IPDF for the fellowship and IITB HPC for the computational facility.

Conflict of Interest

The authors declare no conflict of interest.

Data Availability Statement

The data that support the findings of this study are available in the supplementary material of this article.

Keywords: Oxo-wall concept · high-valent metal-oxo species · ab initio calculations · C − H bond activation · quantum mechanical mixture

[1] a) C. J. Ballhausen, H. B. Gray, *Inorg. Chem.* **1962**, *1*, 111–122; b) J. R. Winkler, H. B. Gray, *Molecular Electronic Structures of Transition Metal Complexes I* **2012**, 17–28.

[2] a) P. R. Ortiz De Montellano, *Cytochrome P450: structure, mechanism, and biochemistry*, Springer Science & Business Media, **2007**; b) X. Huang, J. T. Groves, *Chem. Rev.* **2017**, *118*, 2491–2553; c) T. Mokkawes, T. De Visser, Y. Cao, S. P. De Visser, *Molecules* **2023**, *28*, 6961; d) K.-B. Cho, H. Hirao, S. Shaik, W. Nam, *Chem. Soc. Rev.* **2016**, *45*, 1197–1210; e) R. Ramanan, K. D. Dubey, B. Wang, D. Mandal, S. Shaik, *J. Am. Chem. Soc.* **2016**, *138*, 6786–6797; f) R. P. Hausinger, *The Enzymes* **2023**, *54*, 71–105.

[3] a) S. P. de Visser, Y.-T. Lin, H. S. Ali, U. K. Bagha, G. Mukherjee, C. V. Sastri, *Coord. Chem. Rev.* **2021**, *439*, 213914; b) M. M. Abu-Omar, A. Loaiza, N. Hontzeas, *Chem. Rev.* **2005**, *105*, 2227–2252; c) E. I. Solomon, T. C. Brunold, M. I. Davis, J. N. Kemsley, S.-K. Lee, N. Lehnert, F. Neese, A. J. Skulan, Y.-S. Yang, J. Zhou, *Chem. Rev.* **2000**, *100*, 235–350; d) C. Krebs, D. Galonic Fujimori, C. T. Walsh, J. M. Bollinger Jr, *Acc. Chem. Res.* **2007**, *40*, 484–492; e) K. Ray, F. F. Pfaff, B. Wang, W. Nam, *J. Am. Chem. Soc.* **2014**, *136*, 13942–13958; f) N. P. Dunham, F. H. Arnold, *ACS Catal.* **2020**, *10*, 12239–12255; g) S. P. de Visser, *Chem. Rec.* **2018**, *18*, 1501–

1516; h) D. D. Malik, W. Ryu, Y. Kim, G. Singh, J.-H. Kim, M. Sankaralingam, Y.-M. Lee, M. S. Seo, M. Sundararajan, D. Ocampo, *J. Am. Chem. Soc.* **2024**, *146*, 13817–13835; i) D. D. Malik, Y. M. Lee, W. Nam, *Bulletin of the Korean Chemical Society* **2022**, *43*, 1075–1082; j) B. Wang, Y.-M. Lee, W.-Y. Tcho, S. Tussupbayev, S.-T. Kim, Y. Kim, M. S. Seo, K.-B. Cho, Y. Dede, B. C. Keegan, *Nat. Commun.* **2017**, *8*, 14839.

[4] a) H. B. Gray, *CI.* **2019**, *41*, 16–19; b) H. B. Gray, J. R. Winkler, *Acc. Chem. Res.* **2018**, *51*, 1850–1857; c) K. P. O'Halloran, C. Zhao, N. S. Ando, A. J. Schultz, T. F. Koetzle, P. M. Piccoli, B. Hedman, K. O. Hodgson, E. Bobyr, M. L. Kirk, *Inorg. Chem.* **2012**, *51*, 7025–7031.

[5] a) V. A. Larson, B. Battistella, K. Ray, N. Lehnert, W. Nam, *Nat. Rev. Chem.* **2020**, *4*, 404–419; b) J. Yang, H. T. Dong, M. S. Seo, V. A. Larson, Y.-M. Lee, J. Shearer, N. Lehnert, W. Nam, *J. Am. Chem. Soc.* **2021**, *143*, 16943–16959.

[6] a) X.-P. Zhang, A. Chandra, Y.-M. Lee, R. Cao, K. Ray, W. Nam, *Chem. Soc. Rev.* **2021**, *50*, 4804–4811; b) Y. F. Su, W. Z. Luo, W. Q. Lin, Y. B. Su, Z. J. Li, Y. J. Yuan, J. F. Li, G. H. Chen, Z. Li, Z. T. Yu, *Angew. Chem.* **2022**, *134*, e202201430; c) H.-Y. Du, S.-C. Chen, X.-J. Su, L. Jiao, M.-T. Zhang, *J. Am. Chem. Soc.* **2018**, *140*, 1557–1565; d) J. G. McAlpin, Y. Surendranath, M. Dinca, T. A. Stich, S. A. Stoian, W. H. Casey, D. G. Nocera, R. D. Britt, *J. Am. Chem. Soc.* **2010**, *132*, 6882–6883.

[7] T. M. Anderson, W. A. Neiwert, M. L. Kirk, P. M. Piccoli, A. J. Schultz, T. F. Koetzle, D. G. Musaev, K. Morokuma, R. Cao, C. L. Hill, *Sci.* **2004**, *306*, 2074–2077.

[8] A. Sen, G. Rajaraman, *Faraday Discuss.* **2022**, *234*, 175–194.

[9] a) M. M. Maltempo, T. H. Moss, M. A. Cusanovich, *Biochim. Biophys. Acta, Protein Struct.* **1974**, *342*, 290–305; b) M. Maltempo, T. Moss, *Q. Rev. Biophys.* **1976**, *9*, 181–215.

[10] a) K. Ray, F. Heims, F. F. Pfaff, *Eur. J. Inorg. Chem.* **2013**, *2013*, 3784–3807; b) A. Decker, E. I. Solomon, *Curr. Opin. Chem. Biol.* **2005**, *9*, 152–163.

[11] A. Sen, A. Ansari, A. Swain, B. Pandey, G. Rajaraman, *Inorg. Chem.* **2023**, *62*, 14931–14941.

[12] a) N. S. Liebov, S. Gu, B. A. McKeown, X. Huang, N. C. Boaz, T. Brent Gunnoe, J. T. Groves, *Computational Materials, Chemistry, and Biochemistry: From Bold Initiatives to the Last Mile: In Honor of William A. Goddard's Contributions to Science and Engineering* **2021**, 767–806; b) D. Yue, H. Hirao, *Front. Chem.* **2024**, *12*, 1471741; c) A. Borovik, A. Follmer, *Dalton Trans.* **2023**, *52*; d) G. Mukherjee, J. K. Satpathy, U. K. Bagha, M. Q. E. Mubarak, C. V. Sastri, S. P. de Visser, *ACS Catal.* **2021**, *11*, 9761–9797; e) X. Zhang, Y. Jiang, Q. Chen, S. Dong, Y. Feng, Z. Cong, S. Shaik, B. Wang, *ACS Catal.* **2021**, *11*, 8774–8785; f) S. Shaik, H. Chen, D. Janardanan, *Nat. Chem.* **2011**, *3*, 19–27; g) A. Thibon, J. England, M. Martinho, V. G. Young Jr, J. R. Frisch, R. Guillot, J. J. Girerd, E. Münck, L. Que Jr, F. Banse, *Angew. Chem.* **2008**, *120*, 7172–7175; h) A. B. Sorokin, E. V. Kudrik, D. Bouchu, *Chem. Comm.* **2008**, 2562–2564; i) Y. Sato, M. Okamura, S. Hikichi, *Eur. J. Inorg. Chem.* **2023**, *26*, e202200728; j) M. Puri, L. Que Jr, *Acc. Chem. Res.* **2015**, *48*, 2443–2452; k) R. A. Baglia, C. M. Krest, T. Yang, P. Leeladee, D. P. Goldberg, *Inorg. Chem.* **2016**, *55*, 10800–10809.

[13] a) D. F. Leto, A. A. Massie, D. B. Rice, T. A. Jackson, *J. Am. Chem. Soc.* **2016**, *138*, 15413–15424; b) M. Suga, F. Akita, M. Sugahara, M. Kubo, Y. Nakajima, T. Nakane, K. Yamashita, Y. Umena, M. Nakabayashi, T. Yamane, *Nat.* **2017**, *543*, 131–135; c) M. Suga, F. Akita, K. Yamashita, Y. Nakajima, G. Ueno, H. Li, T. Yamane, K. Hirata, Y. Umena, S. Yonekura, *Sci.* **2019**, *366*, 334–338; d) P. E. Siegbahn, *Acc. Chem. Res.* **2009**, *42*, 1871–1880; e) D. A. Pantazis, W. Ames, N. Cox, W. Lubitz, F. Neese, *Angew. Chem. Int. Ed.* **2012**, *51*, 9935–9940; f) I. Dance, *Dalton Trans.* **2015**, *44*, 18167–18186; g) T. Malcomson, F. Rummel, M. Barchenko, P. O'Malley, *J Photochem Photobiol B.* **2024**, 112946; h) I. Dance, *Dalton Trans.* **2025**; i) P. E. Siegbahn, *Phys. Chem. Chem. Phys.* **2018**, *20*, 22926–22931.

[14] M. Srnec, S. D. Wong, M. L. Matthews, C. Krebs, J. M. Bollinger Jr, E. I. Solomon, *J. Am. Chem. Soc.* **2016**, *138*, 5110–5122.

[15] D. Kim, J. Cho, Y. M. Lee, R. Sarangi, W. Nam, *Chem. Eur. J.* **2013**, *19*, 14112–14118.

[16] a) Y. Suh, M. S. Seo, K. M. Kim, Y. S. Kim, H. G. Jang, T. Tosha, T. Kitagawa, J. Kim, W. Nam, *J. Inorg. Biochem.* **2006**, *100*, 627–633; b) F. Namuswe, T. Hayashi, Y. Jiang, G. D. Kasper, A. A. N. Sarjeant, P. Moënne-Loccoz, D. P. Goldberg, *J. Am. Chem. Soc.* **2010**, *132*, 157–167; c) P. Comba, G. Velmurugan, *Eur. J. Inorg. Chem.* **2025**, e202400837.

[17] E. Kraka, J. A. Larsson, D. Cremer, *Computational Spectroscopy; Grunenberg, J., Ed.; Wiley: New York, NY, USA* **2010**, 105–149.

[18] a) M. Guo, M. S. Seo, Y.-M. Lee, S. Fukuzumi, W. Nam, *J. Am. Chem. Soc.* **2019**, *141*, 12187–12191; b) R. S. Czernuszewicz, Y. O. Su, M. K. Stern, K. A. Macor, D. Kim, J. T. Groves, T. G. Spiro, *J. Am. Chem. Soc.* **1988**, *110*, 4158–4165; c) S. H. Kim, H. Park, M. S. Seo, M. Kubo, T. Ogura, J. Klajn, D. T. Gryko, J. S. Valentine, W. Nam, *J. Am. Chem. Soc.* **2010**, *132*, 14030–14032; d) B. S. Mandimutsira, B. Ramdhanie, R. C. Todd, H. Wang, A. A. Zareba, R. S. Czernuszewicz, D. P. Goldberg, *J. Am. Chem. Soc.* **2002**, *124*, 15170–15171; e) H.-A. Chu, W. Hillier, N. A. Law, G. T. Babcock, *Biochim. Biophys. Acta, Bioenerg.* **2001**, *1503*, 69–82.

[19] a) J. B. Gordon, T. Albert, A. Dey, S. Sabuncu, M. A. Siegler, E. Bill, P. Moënne-Loccoz, D. P. Goldberg, *J. Am. Chem. Soc.* **2021**, *143*, 21637–21647; b) G. L. Tripodi, M. M. Dekker, J. Roithová, L. Que Jr, *Angew. Chem. Int. Ed.* **2021**, *60*, 7126–7131; c) D. C. Lacy, R. Gupta, K. L. Stone, J. Greaves, J. W. Ziller, M. P. Hendrich, A. Borovik, *J. Am. Chem. Soc.* **2010**, *132*, 12188–12190.

[20] M. Zhang, M. De Respinis, H. Frei, *Nat. Chem.* **2014**, *6*, 362–367.

[21] M. Borrell, E. Andris, R. Navrátil, J. Roithová, M. Costas, *Nat. Commun.* **2019**, *10*, 901.

[22] S. Pattanayak, A. J. Jasniewski, A. Rana, A. Draksharapu, K. K. Singh, A. Weitz, M. Hendrich, L. Que Jr, A. Dey, S. Sen Gupta, *Inorg. Chem.* **2017**, *56*, 6352–6361.

[23] a) K. M. Van Heuvelen, A. T. Fiedler, X. Shan, R. F. De Hont, K. K. Meier, E. L. Bominaar, E. Münck, L. Que Jr, *Proc. Natl. Acad. Sci. U. S. A.* **2012**, *109*, 11933–11938; b) J. Chen, H. Yoon, Y.-M. Lee, M. S. Seo, R. Sarangi, S. Fukuzumi, W. Nam, *Chem. Sci.* **2015**, *6*, 3624–3632; c) S. A. Cook, A. S. Borovik, *Acc. Chem. Res.* **2015**, *48*, 2407–2414.

[24] a) Q. Zhang, A. Bell-Taylor, F. M. Bronston, J. D. Gorden, C. R. Goldsmith, *Inorg. Chem.* **2017**, *56*, 773–782; b) C. Panda, A. Chandra, T. Corona, E. Andris, B. Pandey, S. Garai, N. Lindenmaier, S. Künstner, E. R. Farquhar, J. Roithová, *Angew. Chem. Int. Ed.* **2018**, *57*, 14883–14887.

[25] a) W. Rasheed, A. Draksharapu, S. Banerjee, V. G. Young Jr, R. Fan, Y. Guo, M. Ozerov, J. Nehrkorn, J. Krzystek, J. Telser, *Angew. Chem.* **2018**, *130*, 9531–9535; b) S. Rana, J. P. Biswas, A. Sen, M. Clémancey, G. Blondin, J.-M. Latour, G. Rajaraman, D. Maiti, *Chem. Sci.* **2018**, *9*, 7843–7858; c) Y. Li, R. Singh, A. Sinha, G. C. Lisensky, M. Haukka, J. Nilsson, S. Yiga, S. Demeshko, S. J. Gross, S. Dechert, *Inorg. Chem.* **2023**, *62*, 18338–18356.

Manuscript received: October 15, 2024
Accepted manuscript online: February 21, 2025
Version of record online: March 5, 2025